Investigation of properties of superfluid ⁴He turbulence using a hot-wire signal

P. Diribarne ⓘ, M. Bon Mardion, A. Girard, J.-P. Moro, and B. Rousset ⓘ
University of Grenoble Alpes, IRIG-DSBT, F-38000 Grenoble, France

F. Chilla and J. Salort ⓘ
University of Lyon, ENS de Lyon, Claude Bernard University, CNRS, Laboratoire de Physique, Lyon, France

A. Braslau, F. Daviaud, B. Dubrulle ⓘ, B. Gallet, I. Moukharski, and E.-W. Saw
Laboratoire SPHYNX, CEA/IRAMIS/SPEC, CNRS URA 2464, F-91191 Gif-sur-Yvette, France

C. Baudet
CNRS, LEGI, F-38041 Grenoble, France

M. Gibert ⓘ, P.-E. Roche ⓘ, and E. Rusaouen
Univ. Grenoble Alpes, Institut NEEL, F-38042 Grenoble, France

Andrei Golov
Department of Physics and Astronomy, The University of Manchester,
Manchester MP13 9PL, United Kingdom

Victor L'vov
Department of Chemical and Biological Physics, Weizmann Institute of Science, 7610001 Rehovot, Israel

Sergey Nazarenko ⓘ
Institut de Physique de Nice, Université Nice-Sophia Antipolis, Parc Valrose, 06108 Nice, France

We report hot-wire measurements performed in two very different, co- and counterrotating flows, in normal and superfluid helium at 1.6 K, 2 K, and 2.3 K. As recently reported, the power spectrum of the hot-wire signal in superfluid flows exhibits a significant bump at high frequency [Diribarne *et al.*, Phys. Rev. B **103**, 144509 (2021)]. We confirm that the bump frequency does not depend significantly on the temperature and further extend the previous analysis of the velocity dependence of the bump, over more than one decade of velocity. The main result is that the bump frequency depends on the turbulence intensity of the flow, and that using the turbulent Reynolds number rather than the velocity as a control parameter collapses results from both co- and counterrotating flows. The vortex shedding model previously proposed, in its current form, does not account for this observation. This suggests that the physical origin of the bump is related to the small scale turbulence properties of the flow. We finally propose some qualitative physical mechanism by which the smallest structures of the flow, at intervortex distance, could affect the heat flux of the hot wire.

I. INTRODUCTION

One of the main questions in the theory of turbulence is how energy is distributed over length scales, i.e., what is, in the k space, the energy spectrum $\mathcal{E}(k)$. It is generally believed that for mechanically driven quantum turbulence, the quantization of vortex circulation is unimportant at scales greater than the mean distance between the superfluid vortex lines, δ, simply called intervortex distance hereafter. Thus, the kinetic energy spectrum at such scales is distributed similarly to the one in classical turbulence. For example, in homogeneous isotropic fully developed turbulence one expects classical Kolmogorov-1941 (K41) spectrum $\mathcal{E}_{K41}(k) \propto k^{-5/3}$ and this is actually what measurements in turbulent superfluid flows show [1,2].

In inertially driven flows, the main differences between the quantum and classical turbulence is expected to arise at scales smaller than δ. However, accessing both the large and the small scale parts of the spectrum simultaneously is an experimental challenge. Large devices, such as SHREK [3], help solving part of the problem by providing a way to have both developed turbulence and still reasonably large inter-vortex length scales, of the order of a hundred micron at the smallest Reynolds number. Still, in those conditions, the proven Eulerian velocity and vorticity sensors operating in He II are in resolution limits.

For example, in a recent paper, Salort *et al*. [4] have analyzed velocity spectra, obtained in the SHREK von Kármán apparatus [3], based on cantilever and "Pitot tube" signals. They reported two different kinds of behavior associated to normal and superfluid conditions, in the limit of very low velocities, where the sensors had a sufficient temporal and spacial resolution to resolve the high k end of the Kolmogorov spectrum. They used a hot wire as a reference anemometer in He I, where its behavior is perfectly understood. Hot wires can be designed to have suitable temporal and spatial resolution, (see, e.g., Refs. [5–8]), but the interpretation of their signal in He II is a challenge [9,10]. The main stumbling block is the apparition of a spectral bump at high frequency. Diribarne *et al*. [9] have shown that the bump in the spectral domain is in fact the result of quasi-periodic enhanced heat flux events, called "glitches." The physical origin of those glitches is still not understood but the authors proposed two main leads: (i) the shedding of large scale structures associated to the destabilization of the thermal pattern that forms around the wire, and (ii) the interaction between the thermal boundary layer and the enhanced velocity fluctuations at scales comparable to the intervortex distance. The former is only related, at first order, to the surrounding flow mean velocity, while the latter is expected to depend on the turbulent properties of the flow.

In the present paper, we analyze the signal obtained from a hot wire in He II and compare it to the velocity measurements performed with a dynamic pressure anemometer (named "Pitot tube" hereafter) to arbitrate between those leads and eventually propose alternatives to understand the physical origin of the glitches. We take advantage of the versatility of the SHREK apparatus to submit the hot wire to two main flow configurations, with very different turbulent properties.

The paper is organized as follows: after a presentation of the experimental setup and the different flow configurations in Sec. II, we show the typical shape of the spectra obtained in He I and He II in Sec. III and finally the velocity dependence of the spectral bump frequency is discussed in Sec. IV.

II. EXPERIMENT DESCRIPTION

A. Experimental apparatus

The SHREK facility [3], see Fig. 1, is a superfluid implementation of the Von Karman flow in a cylindrical container of inner diameter $R_s = 39$ cm with two propellers of diameter $R = 38$ cm equipped with blades. The distance between the turbine base disks is $h \approx 70$ cm.

The rotation frequencies f_1 and f_2 of the bottom and top turbine, respectively, can be varied independently in the range 0–2 Hz, which allows to produce a variety of flows from the counterrotating case ($f_1 \times f_2 < 0$) to the corotating flow ($f_1 \times f_2 > 0$). See Fig. 1 for the + rotation direction.
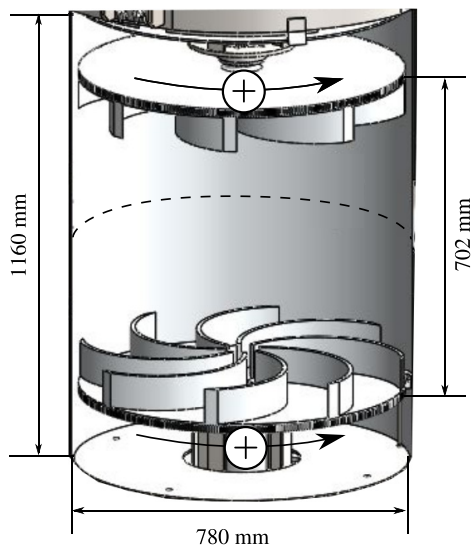
FIG. 1. Schematic view of the SHREK experimental setup [3]. The dashed line marks the equatorial plane, where the sensors are located.

In the present paper, we focus on two kinds of flows: (i) the corotating flow that has the bottom and the top propellers rotating in the same + direction at $f_1 = f2$, (ii) the counterrotating flow that has $f_1 > 0$ and $-2.5 < f_1/f_2 \leqslant -1.1$.

For both flows we explore three different temperatures: $T = 2.3$ K, 2.0 K. and 1.6 K.

To operate hot wires, the pressure $P = 2.5 \pm 0.1$ bar is maintained above the critical pressure.

B. The probes

Here, we describe the two sensors that are used to derive turbulent energy spectra: the pitot tube and the hot wire. Both are placed in the equatorial plane (see dashed line in Fig. 1) at about 4 cm from the wall.

The sensors are oriented in the azimuthal direction, targeting measurements of the θ component of the velocity. However, it is likely that both sensors are also sensitive to the z component of the velocity.

The acquisition frequency is nominally 30 kHz, and data sets are acquired over times of the order of 10^4 large eddy turnover times, allowing for a good statistical convergence.

We would like to emphasize that these two types of sensors were originally proposed for measuring the velocity in classical fluids, mostly at room temperature. Using them in cryogenic conditions, even in the normal fluid, poses new challenges. This is even more problematic in the superfluid regimes. However, using the two types of sensors simultaneously gives a degree of confidence about the consistency of the results at least in the large-scale range, where the normal and superfluid components motions are mostly synchronized by the mutual friction.

In the present paper, we have chosen not to present the results obtained with yet another probe, a cantilever, because this probe was located at a different distance from the wall with potentially different flow properties.

1. The hot wire

The hot wire is prepared from a commercial so-called "Wollaston wire" (see Ref. [10] for details). The sensitive part, made of a 90% Platinum 10% Rhodium alloy, is 1.3 μm in diameter and 300 μm

in length. It is etched by electro-erosion in a 35% nitric acid solution. The whole wire is soldered on a DANTEC 55P01 hot-wire support.

We operate the sensor using a commercial DISA 55-M10 constant temperature anemometer. This allows us to monitor the power needed to overheat the wire at a fixed temperature $T_w \approx 25\,\mathrm{K}$.

In He I, as in standard fluids, the measurement principle is based on the enhancement of heat transfer with forced convection. The velocity fluctuations at length scales larger than the length of the wire can be directly deduced from the power signal, by means of a standard King's calibration law:

$$e^2 = a + bv^{1/2}, \tag{1}$$

where e is the anemometer voltage and v is the velocity of the liquid He I flowing around the wire.

However, in He II, the interpretation of the power signal is trickier. The efficiency of the heat transfer is also enhanced by forced convection and the large scale velocity fluctuations, at small frequency, can still be deduced from the signal [10]. At higher frequency though, the signal is marked by a spectral bump which cannot directly be attributed to velocity fluctuations in the flow but rather to short-lived intense cooling events, called "glitches," lasting typically less than a millisecond [9].

Since the hot-wire temperature is larger than T_λ, it is surrounded by a thin boundary layer of He I. Actually it is the presence of this He I layer that allows for the sensitivity to velocity [9]. Out of this layer, in He II, the heat flux drives an intense counterflow which, in turn, generates additional small-scale turbulence in the form of a dense tangle of quantized vortex lines.

2. The Pitot tube

In classical fluid, the Pitot tube gives access to the dynamic pressure $s(t) = \rho v(t)^2/2$, where ρ is the density of the liquid and v is velocity, by measuring the pressure difference between the stagnation pressure, at the nozzle facing the flow, and the static pressure at an opening perpendicular to the flow (see Ref. [4] for technical details). Below the superfluid transition, this sensing principle remains valid at flow scales resolved by the present sensor, because the superfluid and the normal fluid have a common velocity at these scales. A new "all sensor and no neck" design is used [11,12], increasing the mechanical resonance of the sensor to about 500 Hz. This upper frequency resolution could be further but it would be at the expense of sacrificing the sensitivity. The readout was capacitive and cross-band spectral averaging [13] was implemented.

C. Flow properties

In this section we first describe the topology of the two flow configurations that we used, namely the corotating and counterrotating flows. Then the hot-wire measurements performed in He I at 2.3 K are used to assess the integral length scale and turbulence intensity in both configurations.

1. Topology

Prior to any measurements in helium, we have explored the flow topology and properties in a scale 1:4 experiment (denoted SPHYNX hereafter), filled with water, using a two components laser Doppler velocimetry (LDV) apparatus. The mean z and θ components of the velocity measured in water are shown in Fig. 2. The radial v_r component (not shown) is deduced from the other two components using the incompressibility condition. Besides a large scale global rotation, in the direction of the impeller rotation, one also observes a vertical circulation, resulting from the blades curvature that induce a pumping. The vertical circulation is descending in the core of the cylinder, and ascending (by incompressibility) at the wall, resulting in a inhomogeneous large vertical shear. In the region where the hot-wire and Pitot measurements are performed, at $r/R \approx 0.9$, the ratio between the azimuthal and vertical components is $v_z/v_\theta \leqslant 4\%$.
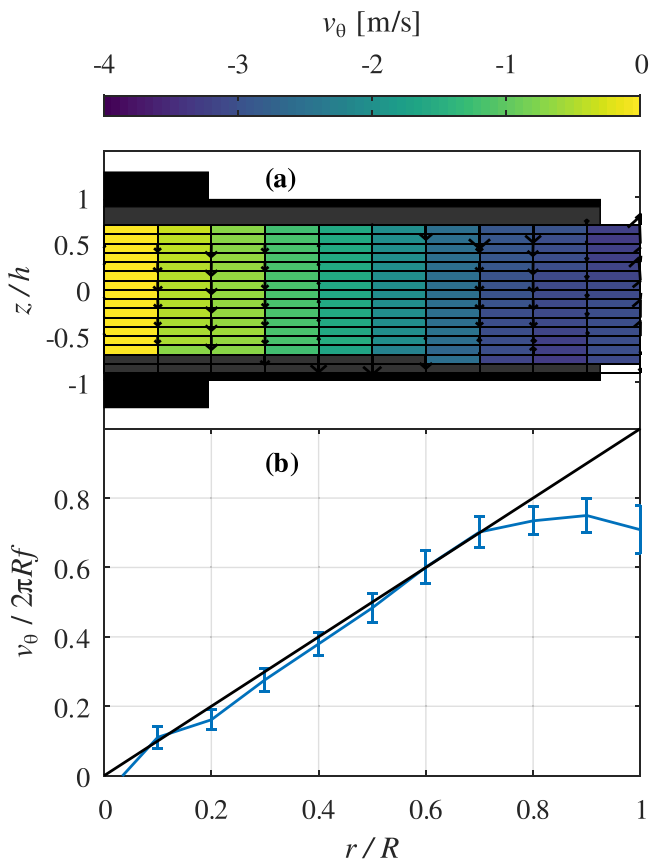
FIG. 2. Azimuthal velocity v_θ of the corotation flow obtained in the SPHYNX water experiment using LDV measurements: (a) Color map of v_θ in the (r, z) plane. Black and gray areas represent the turbines disk and blades, respectively. Arrows indicate the amplitude of the vertical velocity v_z, of which the maximum is approximately 4% of $v_\theta(r/R = 1)$. (b) v_θ normalized by the velocity at the tip of the turbines ($2\pi R f$) averaged over the height of the flow. The error bars show the standard deviation of the azimuthal velocity.

In the counterrotation case, the flow is divided into two toric cells separated by an azimuthal shear layer, in which the mean azimuthal velocities are zero. The position of the shear layer depends on the ratio $|f_1|/|f_2|$: it is at equidistance from the two impellers if $|f_1| = |f_2|$, and shifted upwards (respectively, downwards) if $|f_1| > |f_2|$ (respectively, $|f_1| < |f_2|$) [14–18]. Therefore, in this paper, we only explore situations where the rotation frequencies of the impellers are shifted ($|f_1| > |f_2|$) to make sure that the average θ component of the velocity is non null. Otherwise, the interpretation of the Pitot and hot-wire signals would not be possible.

Figure 3 shows the calibration of the hot-wire voltage e_{wire} in the corotation and counterrotation cases. In absence of a reference velocity measurement in SHREK, we assumed in both cases that the azimuthal velocity was of the form

$$v_\theta = \alpha 2\pi R f_1. \tag{2}$$

In corotation, previous measurement in SPHYNX [see Fig. 2(b)] suggest that using $\alpha \approx 0.75$ is a reasonable assumption. We thus choose to take $\alpha = 0.75$ for the corotation case and search the value of α in the counterrotating case that leads to the best match of the mean hot-wire voltage for a given velocity. We find that, in counterrotation, $\alpha \approx 0.45$, i.e., that the velocity at the sensors location is 45% the velocity at the tip of the fastest turbine.
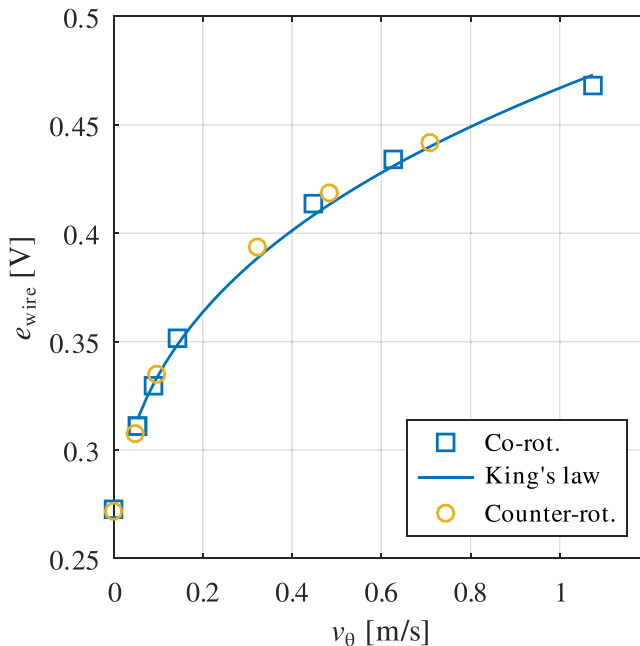
FIG. 3. Mean voltage of the hot-wire anemometer as a function of the velocity v_θ defined as $v_\theta = \alpha 2\pi R f_1$ where $\alpha = 0.75$ in the corotation case and $\alpha = 0.45$ in the counterrotation case. The solid line is a fit of the corotation data using the King's law; see Eq. (1).

2. Turbulence properties

The turbulence properties of the flow are estimated both in the SPHYNX experiment using LDV and in SHREK using the hot-wire measurements in He I.

a. Turbulence intensity. The turbulence intensity τ defined as the ratio

$$\tau = \sigma_v/|\mathbf{v}|,$$

where $\mathbf{v} = v_\theta \mathbf{e}_\theta + v_z \mathbf{e}_z$ and $\sigma_v = \sqrt{\langle v'^2 \rangle}$ is the standard deviation of the module of the velocity $\mathbf{v}$. At a distance of order 4 cm from the wall, i.e., at coordinate $r/R \approx 0.9$ in Fig. 2(b), the turbulence intensity is found to be in the range 5–10%. This order of magnitude is confirmed by hot-wire measurements in corotating He I, where the inferred value is $\tau \approx 5.2\%$ [4]. Using the same technique, and the calibration from Fig. 3 one finds $\tau \approx 22\%$ in counterrotation, i.e., a turbulence intensity which is 4–5 times larger than in corotation.

b. Integral length scale. We used the hot-wire velocity signal to compute the longitudinal integral length scale L_l defined as

$$L_l = \int_0^{+\infty} \frac{\langle v'(0)v'(r) \rangle}{\langle v'^2 \rangle} d(\delta r).$$

As shown in Ref. [4] this leads to $L_l \approx 2.9$ cm in corotation, while we find $L_l \approx 3.7$ cm in the counterrotation case.

III. LOCAL ENERGY SPECTRA

In this section we present power spectral density of the hot-wire signal in both co- and counter-rotating flows.
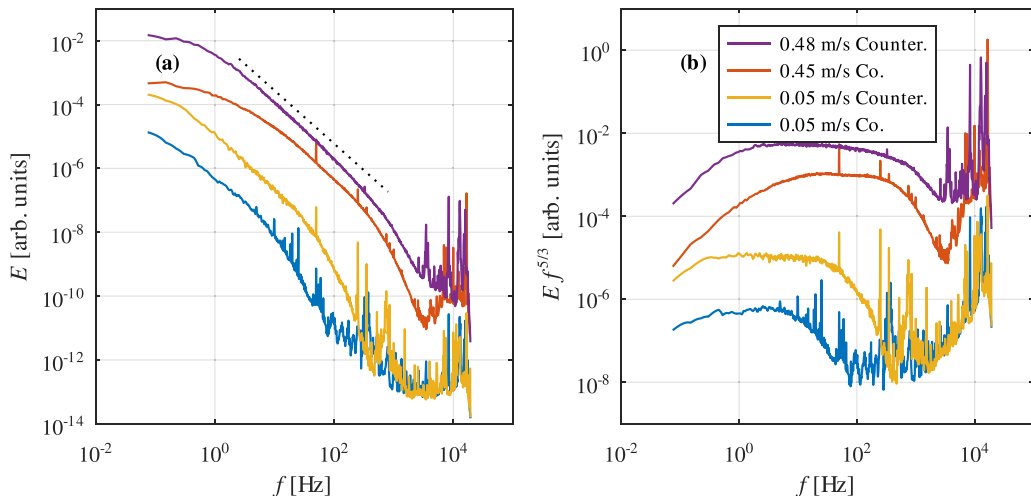
FIG. 4. (a) Power spectral density of the hot-wire signal in He I at 2.3 K. Amplitudes are shifted arbitrarily for better readability. The dotted lines show a $f^{-5/3}$ power law. (b) Same spectra compensated by $f^{5/3}$.

Since the large scale behavior of those flows is not expected to be affected by the transition to superfluid phase [1,17], we first present measurements in He I where the hot wire is expected to behave as a standard anemometer. Those spectra are further used as references and compared to those obtained in He II.

A. Normal fluid

Figure 4(a) shows the power spectral density (PSD hereafter) of the hot-wire signal in corotation and in counterrotation at two comparable azimuthal velocities. To make sense out of those spectra we assume the Taylor hypothesis of frozen turbulence, so that we can translate a given frequency f to a length scale l through the relation $l = \langle v_\theta \rangle / f$. Note though that this hypothesis is probably not justified in the case of counterrotation, where the turbulence intensity is very high, but this should only matter at the highest frequencies.

The spectra are flat at low frequency and then tend to follow a power law at higher frequency, where the inertial range of length scales is expected to lie. At even higher frequency a cutoff is observed. The compensated spectra in Fig. 4(b) show that the power law in the inertial range is compatible with a Kolmogorov $f^{-5/3}$ energy cascade in both flows. The transition from the low-frequency uncorrelated flat spectrum to the power law is quite different in corotation and in counterrotation though. Since the integral length scales are comparable in both flows, we expect that the transition happens at comparable frequency for a given azimuthal velocity. Even though the transition from flat to power law behavior actually seems to happen at comparable frequencies, in counterrotation it is much more steep than in corotation where the slope evolves gradually from 0 to $-5/3$ over a decade of frequencies.

The interpretation of the cutoff at large frequency calls for caution. At low velocity, it happens at lower frequency in the corotating than in the counterrotating case. If the cutoff marks the beginning of the dissipative length scales, this is expected since the turbulence intensity of the latter is much higher than the former. At high velocity though, we can hardly distinguish the cutoff frequencies and it is likely that it should be attributed to a finite size effect.

B. Superfluid

Figure 5(a) compares the PSD of the hot-wire raw signal in He I (2.3 K) and in He II (2 K) in corotation at low velocity. In He II, we see that a large spectral bump appears at high frequencies,
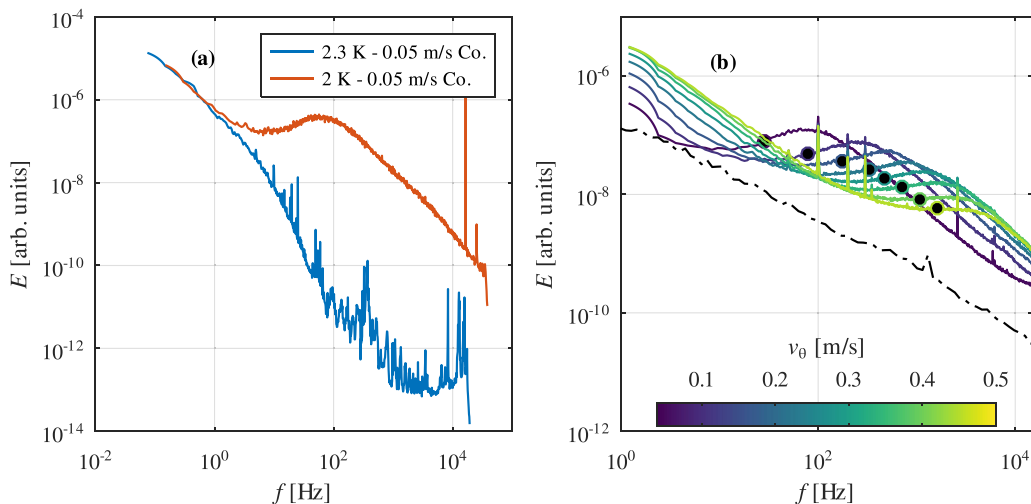
FIG. 5. (a) Power spectral density of the hot-wire signal in He I (2.3 K) and in He II (2 K) in corotation at 0.07 m/s. Amplitudes are shifted so that the spectra match at low frequency. (b) Series of spectra in He II (2 K) in corotation at velocities varying in the range 0.04–0.45 m/s (colored solid lines) and at 0 m/s (black dash dotted). The black dots mark the inflection point in the high-frequency bump.

where, in He I, the PSD is already damped by the viscous cutoff. This spectral bump is actually associated with short-lived heat flux enhancement events that account for a significant, velocity dependent, portion of the variance of the hot-wire signal. Thus velocity fluctuations cannot be directly inferred from the hot-wire raw signal.

In Fig. 5(b) we show PSD obtained in He II (2 K) at increasing azimuthal velocities, in corotation flow. It is clear that the frequency at which the spectral bump appears increases with the flow velocity. In quiescent helium, no bump is observed, down to the lowest resolved frequencies. Those features have also been reported in Ref. [9] but within a more limited range of velocities and in a grid flow where the turbulence intensity is very low (less than 2%). Note that, contrary to previous observations, while at low velocity a local maximum is observed, at high velocity the bump takes the form of departure from the low-frequency power-law behavior with no clear extremum.

C. Comparison with Pitot-velocity spectra

While the Pitot tube has a lower spatial resolution, the interpretation of its signal is more straightforward. Especially in the case of the corotation flow, where the turbulence intensity is low, the Pitot signal fluctuations can be shown to be linearly related to velocity fluctuations in the flow.

Figure 6 shows a comparison of the Pitot and hot-wire signal PSD in corotation. In He I, the shape of the PSD of the two sensors are very similar at low frequencies: after a nonuniversal shallower spectrum at low frequencies, the PSD shows a $f^{-5/3}$ power law from $f \approx 5$ Hz up to $f \approx 20$ Hz where the spectrum reaches a noise plateau. The latter can be explained by the low sensitivity of the Pitot sensor at low velocity. The peak in the Pitot spectrum at $f \approx 540$ Hz is due to the probe mechanical resonance.

As shown by Salort *et al.* [4], in He II at the same velocity, the PSD of the Pitot remains unchanged up to $f \approx 3$ Hz where a departure is observed: instead of tending to a $f^{-5/3}$ power law like in He I, the PSD amplitude keeps decreasing like $\sim f^{-1}$ until it reaches the tail of the probe mechanical peak, at $f \approx 200$ Hz.

A departure from the He I PSD is also observed at approximately the same frequency (around 3 Hz) but it is not as pronounced as for the hot wire.
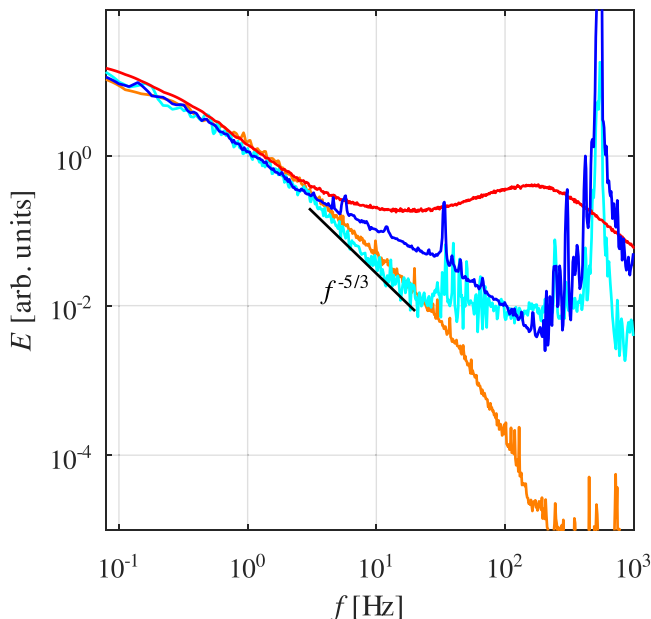
FIG. 6. Comparison of the Pitot and hot-wire signal spectra, E, at 2.3 K (cyan and orange, respectively) and 2 K (blue and red, respectively) in corotation at 0.09 m/s. The solid black lines shows a $f^{-5/3}$ power law. An arbitrary scaling factor is applied so that the amplitudes match at 1 Hz.

This departure in the Pitot spectrum is attributed to the pile-up of kinetic energy in the superfluid component in the near dissipative range of length scales [4,19].

IV. DISCUSSION

In this section we will to try explain the shape of the hot-wire spectra and underpin the origin of the high-frequency bump in the hot-wire signal.

A. Velocity dependence

To analyze the velocity dependence of the high-frequency bump in the hot-wire signal, we define the representative frequency f_{bump} as the local inflection point between the low-frequency power law and the high-frequency spectral departure [see the black dots in Fig. 5(b)]. Contrary to previous studies, the bump here does not always feature a maximum, and this definition guaranties that we can always find a representative frequency for the bump. Qualitatively, f_{bump} can be viewed as the lowest frequency at which the bump starts.

The inflection point is located automatically by first fitting the PSD at intermediate frequencies with a third order polynomial and looking for a local maximum in the derivative dE/df.

Figure 7(a) shows f_{bump} as a function of the azimuthal velocity v_θ for both corotation and counterrotation cases at 2 and 1.6 K. The representative frequency is extracted either from experiments at steady or at very slowly ($\approx 1 \times 10^{-5}$ Hz s^{-1}) varying turbine frequency. In the case of varying frequency, each point is extracted from a spectrum averaged over ten consecutive datasets lasting ≈ 54 s each (about 800 integral times at the smallest rotation frequency). Only points for which the turbine frequency varies of 15% at most between the first and the last dataset are shown.

From this figure, one already notices two striking features:

(i) the bump appears at higher frequency in counterrotation (round markers) than in corotation (square markers) for a given azimuthal velocity,
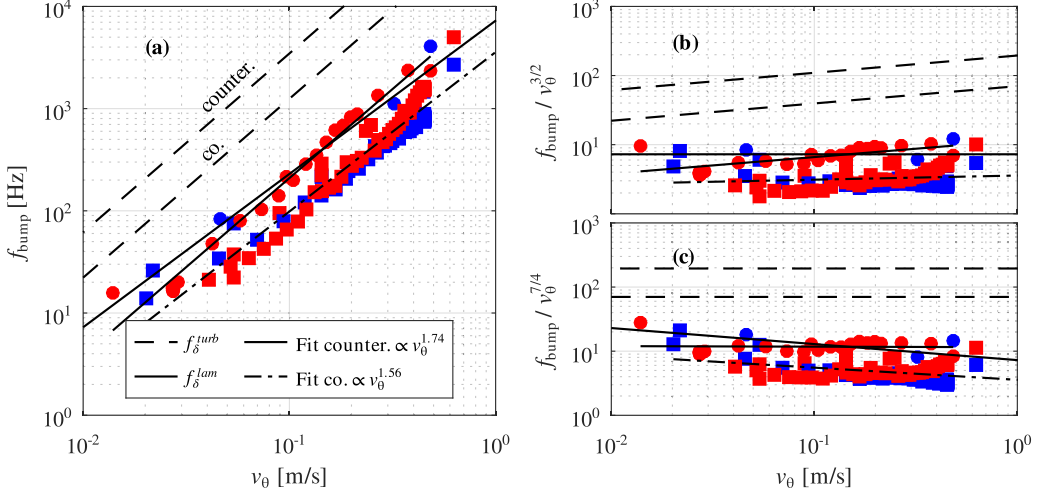
FIG. 7. Representative frequency of the spectral bump f_{bump} as a function of the azimuthal velocity v_θ in counterrotation (square symbols) and corotation (round symbols) at 2 K (red) and 1.6 K (blue). The solid and dash-dotted black lines show the best fit of the form $f_{\text{bump}} \propto v_\theta^\gamma$ for the counterrotating and corotating cases, respectively. The dashed lines correspond to f_δ^{turb} computed from Eq. (7) for both kinds of flows, while the dotted line corresponds to f_δ^{lam}, Eq. (5). (a) Raw frequency. (b) Frequency divided by $v_\theta^{3/2}$. (c) Frequency divided by $v_\theta^{7/4}$.

(ii) the bump frequency does not significantly depend on the temperature (red versus blue markers).

The bump is not visible in quiescent fluid at the resolved frequencies [see Fig. 5(b)]. It is therefore reasonable to assume that f_{bump} tends to 0 Hz when the velocity tends to 0 m/s. The investigation of the emergence of the bump in the low velocity limit would require a dedicated campaign with very large acquisition times, and is beyond the scope of this paper. In the range of velocities investigated here, the velocity dependence of the bump frequency can be represented as a simple power law. The solid and dash-dotted black lines in Fig. 7 indicate, in counterrotation and in corotation, respectively, the best fits of the form

$$f_{\text{bump}} \propto v_\theta^\gamma. \tag{3}$$

The exponent γ is higher in counterrotation ($\gamma = 1.74$) than in corotation ($\gamma = 1.56$). Note that since the estimated azimuthal velocity in counterrotation is calibrated against that in corotation, the observed difference cannot be attributed to a wrong value for α in Eq. (2). Anyway, the velocity range here is about 1.5 decades, much larger than in previous studies [9], which strongly supports the view that the bump frequency dependence with the velocity is steeper than a simple linear dependence.

We identify below some of the relevant characteristic frequencies that can emerge in a rotating turbulent flow and we detail their respective velocity dependence.

a. Vortex-streets emanating from the wire. Diribarne *et al.* [9] have shown that the normal and superfluid components form two well defined "winglike" patterns in the vicinity of the wire. The characteristic size of the patterns, was shown to be typically hundred times the diameter of the wire in their working conditions. They further argue that this flow pattern should be unstable and could lead to Kármán vortex streets in the wake of the "wing." Assuming the hot-wire heat flux is affected by this vortex shedding, this would lead to a frequency:

$$f_{\text{Kármán}} = \frac{2\text{St}v_\theta}{D(T, v_\theta)}, \tag{4}$$

where St is the Strouhal number [20] of the order 0.1–0.3, and $D(T, v_\theta)$ is the temperature- and velocity-dependent characteristic size of the thermal wing pattern. The dependence of D on the velocity has been shown to be of the order $\propto v_\theta^{-1}$ in cylindrical approximation, and to tend toward $\propto v_\theta^{-1/2}$ when D becomes large as compared to the length of the wire. It thus predicts a vortex shedding frequency $f_{\text{Kármán}} \propto v_\theta^\beta$ with $1.5 \lesssim \beta \lesssim 2$.

b. Frequency corresponding to intervortex distance. Because turbulence in SHREK is inhomogeneous, the intervortex distance is expected to vary depending on the position in the flow. We can derive two limiting formulas for the frequency corresponding to the intervortex distance f_δ, assuming that we are in a corotating laminar flow or a fully turbulent regime. In the first case, we can take as a reference the distance between the vortex neighbors in a laminar superfluid uniformly rotating with frequency f_r, which is likely to be the lower bound since the mean vorticity of the turbulent flow is larger than the one in the laminar flow. In this case, the vortex line density is given by $\mathcal{L} = 4\pi f_r/\kappa$ (see, e.g., Refs. [21,22]) and the intervortex distance by $\delta = \mathcal{L}^{-1/2} = (4\pi f_r/\kappa)^{-1/2}$. Assuming that the vortex array is advected at the same velocity as the mean flow, we consequently find that the typical frequency f_δ^{lam} corresponding to such a reference scale is v_θ/δ, hence

$$f_\delta^{\text{lam}} = \left(\frac{2}{\kappa R}\right)^{1/2} v_\theta^{3/2}. \tag{5}$$

Let us now consider turbulence when estimating the intervortex scale. It has been shown that in the hypothesis of homogeneous and isotropic turbulence (HIT hereafter), the intervortex spacing scales like the Kolmogorov dissipative length scale [19,23]:

$$\frac{\delta}{L_l} = \left(\frac{\nu_{\text{eff}}}{\kappa}\right)^{1/4} \text{Re}_\kappa^{-3/4}, \tag{6}$$

where ν_{eff} is determined experimentally (see, e.g., Refs. [23–25]) and $\text{Re}_\kappa = \sigma_v L_l/\kappa$ is the turbulent Reynolds number. Using the Taylor hypothesis, Eq. (6) translates to a frequency in the Eulerian frame

$$f_\delta^{\text{turb}} = \left(\frac{\tau^3}{\nu_{\text{eff}} L \kappa^2}\right)^{1/4} v_\theta^{7/4}. \tag{7}$$

The vortex shedding model [Eq. (4)] predicts a velocity dependence of the shedding frequency compatible with the data for f_{bump}. However, in this basic model, the amplitude of the velocity fluctuations relative to the mean velocity, i.e., the turbulence intensity, do not play any role and this is in contradiction with the fact f_{bump} is found to have notably different values in the corotating and counterrotating situations for a given mean velocity. Additionally, we expect that in this model, including some fluctuations around the mean velocity would probably increase the standard deviation of the shedding frequency rather than changing its mean value. Moreover, it was shown [9] that due to the temperature dependence of the characteristic thermal pattern size D in Eq. (4), the spectral bump frequency should depend noticeably on the temperature. For those reasons, the shedding model, in its current basic form, seems unable to account for the present measurements.

The frequency associated to the intervortex distance, is expected to scale as $v_\theta^{3/2}$ or $v_\theta^{7/4}$ for the laminar and turbulent cases, respectively. The compensated plots in Figs. 7(b) and 7(c) show that both exponents are good candidates, even though counterrotation data seem to have a slightly steeper slope, as seen from the fits (solid and dashed-dotted line in Fig. 7). The expected frequency f_{bump} for the laminar (dotted line in Fig. 7) and the turbulent (dashed lines in Fig. 7) show that the estimated frequencies, are in qualitative agreement in both cases. The true motion is clearly neither purely laminar nor statistically isotropic: it consists of both (an anisotropic) turbulence and a rotational mean flow. Therefore, the scaling of f_{bump} should be somewhere in between of the purely laminar and the purely turbulent scalings. However, since the latter two scalings are very close to each other, we believe that our conclusion that f_{bump} is associated with the intervortex spacing is robust.
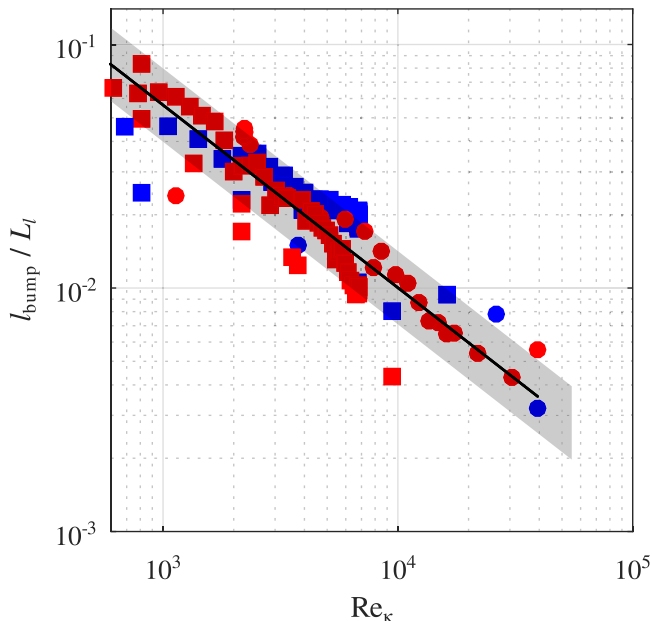
FIG. 8. Characteristic length $l_{bump} = v_\theta / f_{bump}$ normalized by the corresponding flow integral length scale L_l as a function of the turbulent Reynolds number. The black line represents Eq. (6) multiplied by an arbitrary factor 15.

In Fig. 8 we show the characteristic length $l_{bump} = v_\theta / f_{bump}$, normalized by the integral length scale L_l, as a function of the turbulent Reynolds number $\mathrm{Re}_\kappa = \tau v_\theta L_l / \kappa$. This representation collapses the data from both kinds of flows onto a reasonably well defined single power law. For comparison, the black line represents the intervortex distance normalized by the integral length scale, Eq. (6), multiplied by an arbitrary factor 15. In the range of temperatures between 1.6 and 2 K, the effective viscosity ν_{eff} has been shown to not depend significantly on the temperature (see, e.g., the compilation of experimental and numerical data from Ref. [23]) and we consequently used the average reported value $\nu_{eff} \approx \kappa/5$ [23]. As a guide to the eye, the gray area shows the region around this line into which the data are scattered by at most a factor of two.

Even though the data are still scattered, it is reasonable to assume that we should search the origin of the spectral bump in phenomena that are prominent at length scales proportional to the intervortex spacing.

B. Interpretation

In the superfluid thermal boundary layer, the very intense counterflow heat flux results in a dense vortex tangle. The intervortex distance varies radially through the thermal (He II) boundary layer: the heat flux decreases as one gets further from the wire, due to the cylindrical geometry, and so does the vortex line density. So no single length scale can be identified in the thermal boundary layer, but close to the wire, where the temperature gradient is significant, the intervortex distance is orders of magnitude smaller (see Ref. [10]) than that of the bulk surrounding turbulent flow.

Diribarne *et al.* [9] have shown that the spectral bump is actually the result of short-lived intense cooling events named "glitches." They did not devise a mechanism by which those sudden enhancements of the heat transfer could be triggered but envisaged two possible leads: (i) the shedding of vortices passed the wire, (ii) the destabilization of the vortex tangle around the wire due to the bottlenecking, or pile-up of kinetic energy, in the superfluid component at scales comparable with the intervortex distance, as predicted in Ref. [19].

As shown in the previous section, we now have arguments to eliminate (i), due to the dependence of the bump frequency on the turbulence intensity. The apparent independence of the bump frequency on the temperature is another argument against this explanation, as already noted in Ref. [9]. However, we can certainly settle on the fact that the process triggering those glitches should occur at small scales. Lead (ii) is appealing, because the hot-wire bump seems to happen at frequencies comparable with those at which a pile-up of kinetic energy happens, as measured by the Pitot tube (see Fig. 6). This is only qualitative: due to the very limited set of velocities where the Pitot tube has a sufficient spacial resolution to show the pile-up, we cannot prove that there is an actual correlation with the appearance of the spectral bump in the wire signal.

Following lead (ii), a mechanism explaining the influence of the hot-wire signal to quantum intervortex distance in the outerflow is as follows: in a mechanically driven quantum turbulence, the mutual friction between the normal and superfluid components couples their turbulent fluctuations: $u_n(r, t) \approx u_s(r, t)$ at all scales larger than the intervortex scale δ. The resulting turbulent energy spectra of the mechanically driven quantum turbulence for the scales much greater than δ are close to those of the classical hydrodynamic turbulence [1,2,26–30]. However, $u_n(r, t)$ and $u_s(r, t)$ decouple at scales of the order of δ. Roughly, such relative motion of the normal fluid and the superfluid vortex tangle can be viewed as a normal flow past an irregular "grid" made of the quantized vortex lines. Naturally, such a flow produces extra turbulence at the "grid spacing" scale, i.e., at the scales comparable to δ. More precisely, on a microscopic level, the normal fluid is a field of acoustic phonons which scatter off the quantized vortices and thereby acquire spatial inhomogeneity with a characteristic scale of the order of the mean distance between such vortex scatterers. Obviously, the energy of the bump cannot come from "nowhere"; i.e., it could only appear as a result of transfer from the mean relative motion at larger scales. A good candidate for such a mean motion is the thermal counterflow produced by the wire. In this case, the bump is indeed a product of the intrusive nature of the hot wire and, at the same time, its properties are affected by the surrounding turbulent flow. This is a simple and robust qualitative mechanism of the spectral bump creation near the intervortex scale. However, for completeness let us mention another possible mechanism for the spectral bump generation.

A third mechanism could explain the heat flux glitches experienced by the hot wire at frequencies corresponding to the small length scales of the external turbulence: The presence of intense vorticity and pressure structures associated with bundles of quantum vortices. Those objects are the counterpart in quantum turbulence of "vorticity worms" well known in classical turbulence (see, e.g., the pioneering numerical and experimental works Refs. [31,32]). The existence of vortex bundles have been reported in quantum turbulence, both numerically [33] and experimentally [34]. Their typical associated length scale (diameter) was reported to be around two times the intervortex distance in superfluid [33] or four times the Kolmogorov viscous length scale [35]. The pressure signature of superfluid vortex bundles was measured in the SHREK apparatus [34], and the authors evidenced that, here again, no real difference could be made between classical and quantum turbulence. When such a vortical structure impinges the wire, we expect it to polarize the vortex tangle constituting the thermal boundary layer, leading to a change in its effective thermal conductivity. Indeed, it was shown that heat transfer can be modeled by standard counterflow phenomenology. In this framework, the mutual friction force per unit volume between the counterflowing normal and superfluid components, is the key ingredient in the definition of a local conduction function. The latter relates the local temperature gradient ∇T in the He II boundary layer with the heat flux φ and in some way it can be seen as an effective thermal conductivity. A theoretical expression of the conduction function $f(T)$ can be obtained at heat fluxes well above the critical heat flux at which the counterflow becomes turbulent [36,37]:

$$f(T) = C \frac{2\rho \rho_s^3 s^4 T^3}{\gamma^2 B \rho_n \kappa},$$ (8)

where $f(T) = |\varphi|^3/|\nabla T|$ is the conduction function, ρ_n and ρ_s are the normal and superfluid density, respectively, s is the entropy per unit mass, B is a constant of order unity (see, e.g.,

Ref. [38]), γ is defined as $\mathcal{L} = \gamma^2 (\boldsymbol{v_n} - \boldsymbol{v_s})^2$ where $\mathcal{L}$ is the local vortex line density of the counterflow (see Ref. [39]), and C depends on the average angle between the vortex lines and the heat flux. For an isotropic vortex tangle, $C = 3/2$, while this constant tends towards infinity when the vortices are polarized and oriented parallel to the counterflow velocity ($\boldsymbol{v_n} - \boldsymbol{v_s}$). This continuous approach proved efficient in modeling heat transfer from heat wire down to micron scales [9,10]. Knowing the collision frequency of the vortical structures on the wire would help to confirm or invalidate this mechanism. Although we have not been able to find previous studies on this specific question, it seems reasonable to assume that the typical collision timescales are linearly related to the timescales of the smallest flow structures, such as the intervortex one. This would be consistent with the scaling reported in Fig. 8.

V. CONCLUSIONS

In this paper, we report experimental measurements in liquid helium using a hot-wire probe and a pitot tube. These measurements are done in the SHREK facility in both He I and He II, for different levels of corotation or counterrotation. In normal fluid, we use the hot wire to devise the integral length scale and turbulence intensity of both flows. This allows us to compute the turbulent Reynolds number in each case.

In He II the hot-wire signal exhibits a spectral bump at high frequency, of which the representative frequency increases with the velocity v_θ, as previously reported, but also with the turbulence intensity of the flow. We show that the latter cannot be explained satisfactorily by the model of vortex shedding as proposed in Ref. [9].

The velocity dependence is compatible with a power law v_θ^γ over more than one decade of frequencies, with γ in the range $1.5 \lesssim \gamma \lesssim 1.8$. Assuming that the frequency of the quantum bump can be translated to a length scale of the flow by use of the Taylor hypothesis, we have presented the resulting length l_{bump} as a function of the turbulent Reynolds number. This representation collapses data from both corotating and counterrotating flows onto a single power law compatible with $l_{\text{bump}} \propto \delta$.

Thus the phenomenon that triggers the quantum bump must happen at scales proportional to the intervortex distance. We recall that the spectral bump is actually the result of thermal "glitches," short lived heat transfer improvement events, in the time domain. We propose two possible qualitative scenarios that end up destabilizing the wire's thermal boundary layer, leading to fluctuations of its overall thermal resistance:

(i) the interaction between the wire's counterflow and the enhanced velocity fluctuations of the flow,

(ii) the polarization of the vortex tangle of the wire by the vortical structures associated to turbulence.

Those explanations are of course qualitative, and some further numerical and experimental studies are needed to understand the quantitative aspects of the quantum bump generation.

ACKNOWLEDGMENTS

---

[1] J. Maurer and P. Tabeling, Local investigation of superfluid turbulence, Europhys. Lett. **43**, 29 (1998).

[2] J. Salort, C. Baudet, B. Castaing, B. Chabaud, F. Daviaud, T. Didelot, P. Diribarne, B. Dubrulle, Y. Gagne, F. Gauthier, A. Girard, B. Hébral, B. Rousset, P. Thibault, and P.-E. Roche, Turbulent velocity spectra in superfluid flows, Phys. Fluids **22**, 125102 (2010).

[3] B. Rousset, P. Bonnay, P. Diribarne, A. Girard, J. M. Poncet, E. Herbert, J. Salort, C. Baudet, B. Castaing, L. Chevillard, F. Daviaud, B. Dubrulle, Y. Gagne, M. Gibert, B. Hébral, T. Lehner, P.-E. Roche, B. Saint-Michel, and M. Bon Mardion, Superfluid high Reynolds von Kármán experiment, Rev. Sci. Instruments 85, 103908 (2014).

[4] J. Salort, F. Chillà, E. Rusaouën, P.-E. Roche, M. Gibert, I. Moukharski, A. Braslau, F. Daviaud, B. Gallet, E.-W. Saw, B. Dubrulle, P. Diribarne, B. Rousset, M. Bon-Mardion, J.-P. Moro, A. Girard, C. Baudet, V. L'vov, A. Golov, and S. Nazarenko, Experimental signature of quantum turbulence in velocity spectra? New J. Phys. 23, 063005 (2021).

[5] M. Vallikivi and A. J. Smits, Fabrication and characterization of a novel nanoscale thermal anemometry probe, J. Microelectromech. Syst. 23, 899 (2014).

[6] Y. Fan, G. Arwatz, T. Van Buren, D. Hoffman, and M. Hultmark, Nanoscale sensing devices for turbulence measurements, Exp. Fluids 56, 138 (2015).

[7] P. Diribarne, P. Thibault, and P.-E. Roche, Nano-shaped hot wire for ultra-high resolution anemometry in cryogenic helium, Rev. Sci. Instrum. 90, 105004 (2019).

[8] H. Le-The, C. Küchler, A. van den Berg, E. Bodenschatz, D. Lohse, and D. Krug, Fabrication of freestanding Pt nanowires for use as thermal anemometry probes in turbulence measurements, Microsyst. Nanoeng. 7, 28 (2021).

[9] P. Diribarne, B. Rousset, Y. A. Sergeev, J. Valentin, and P.-E. Roche, Cooling with a subsonic flow of quantum fluid, Phys. Rev. B 103, 144509 (2021).

[10] D. Durì, C. Baudet, J.-P. Moro, P.-E. Roche, and P. Diribarne, Hot-wire anemometry for superfluid turbulent coflows, Rev. Sci. Instruments 86, 025007 (2015).

[11] O. Berberig, K. Nottmeyer, J. Mizuno, Y. Kanai, and T. Kobayashi, The prandtl micro flow sensor (pmfs): A novel silicon diaphragm capacitive sensor for flow-velocity measurement, Sens. Actuators, A 66, 93 (1998).

[12] I. Moukharski and A. Braslau, Miniature differential pressure flow sensor, U.S. Patent 10,018,489 (2018).

[13] I. Moukharski, Method and device for reducing noise in a modulated signal, U.S. Patent 20,190,138,572 (2019).

[14] F. Ravelet, Bifurcations globales hydrodynamiques et magnétohydrodynamiques dans un écoulement de von Kármán turbulent, Ph.D. thesis, Ecole Polytechnique X (2005), https://pastel.archives-ouvertes.fr/tel-00011016.

[15] R. Monchaux, F. Ravelet, B. Dubrulle, A. Chiffaudel, and F. Daviaud, Properties of Steady States in Turbulent Axisymmetric Flows, Phys. Rev. Lett. 96, 124502 (2006).

[16] P.-P. Cortet, A. Chiffaudel, F. Daviaud, and B. Dubrulle, Experimental Evidence of a Phase Transition in a Closed Turbulent Flow, Phys. Rev. Lett. 105, 214501 (2010).

[17] B. Saint-Michel, F. Daviaud, and B. Dubrulle, A zero-mode mechanism for spontaneous symmetry breaking in a turbulent von Kármán flow, New J. Phys. 16, 013055 (2014).

[18] S. Thalabard, B. Saint-Michel, E. Herbert, F. Daviaud, and B. Dubrulle, A statistical mechanics framework for the large-scale structure of turbulent von Kármán flows, New J. Phys. 17, 063006 (2015).

[19] J. Salort, P.-E. Roche, and E. Lévêque, Mesoscale equipartition of kinetic energy in quantum turbulence, Europhys. Lett. 94, 24001 (2011).

[20] V. Strouhal, Ueber eine besondere art der tonerregung, Ann. Phys. (Berlin) 241, 216 (1878).

[21] R. Feynman, Application of quantum mechanics to liquid helium, in *Progress in Low Temperature Physics*, Vol. 1, edited by C. Gorter (Elsevier, Amsterdam, 1955), pp. 17–53.

[22] E. J. Yarmchuk, M. J. V. Gordon, and R. E. Packard, Observation of Stationary Vortex Arrays in Rotating Superfluid Helium, Phys. Rev. Lett. 43, 214 (1979).

[23] S. Babuin, E. Varga, L. Skrbek, E. Lévêque, and P.-E. Roche, Effective viscosity in quantum turbulence: A steady-state approach, Europhys. Lett. 106, 24006 (2014).

[24] M. R. Smith, R. J. Donnelly, N. Goldenfeld, and W. F. Vinen, Decay of Vorticity in Homogeneous Turbulence, Phys. Rev. Lett. 71, 2583 (1993).

[25] S. R. Stalp, L. Skrbek, and R. J. Donnelly, Decay of Grid Turbulence in a Finite Channel, Phys. Rev. Lett. 82, 4831 (1999).

[26] C. F. Barenghi, L. Skrbek, and K. R. Sreenivasan, Introduction to quantum turbulence, Proc. Natl. Acad. Sci. USA **111**, 4647 (2014).

[27] J. Salort, B. Chabaud, E. Lévêque, and P. E. Roche, Investigation of intermittency in superfluid turbulence, J. Phys.: Conf. Ser. **318**, 042014 (2011).

[28] P.-E. Roche, C. F. Barenghi, and E. Leveque, Quantum turbulence at finite temperature: The two-fluids cascade, Europhys. Lett. **87**, 54006 (2009).

[29] C. F. Barenghi, V. S. L'vov, and P.-E. Roche, Experimental, numerical, and analytical velocity spectra in turbulent quantum fluid, Proc. Natl. Acad. Sci. USA **111**, 4683 (2014).

[30] V. Eltsov, R. Hänninen, and M. Krusius, Quantum turbulence in superfluids with wall-clamped normal component, Proc. Natl. Acad. Sci. USA **111**, 4711 (2014).

[31] E. D. Siggia, Numerical study of small-scale intermittency in three-dimensional turbulence, J. Fluid Mech. **107**, 375 (1981).

[32] S. Douady, Y. Couder, and M. E. Brachet, Direct Observation of the Intermittency of Intense Vorticity Filaments in Turbulence, Phys. Rev. Lett. **67**, 983 (1991).

[33] A. W. Baggaley, C. F. Barenghi, A. Shukurov, and Y. A. Sergeev, Coherent vortex structures in quantum turbulence, Europhys. Lett. **98**, 26002 (2012).

[34] E. Rusaouen, B. Rousset, and P.-E. Roche, Detection of vortex coherent structures in superfluid turbulence, Europhys. Lett. **118**, 14005 (2017).

[35] J. Jiménez and A. A. Wray, On the characteristics of vortex filaments in isotropic turbulence, J. Fluid Mech. **373**, 255 (1998).

[36] W. F. Vinen, Mutual friction in a heat current in liquid helium II. III. Theory of the mutual friction, Proc. R. Soc. London A **242**, 493 (1957).

[37] S. W. Van Sciver, He II heat and mass transfer, in *Helium Cryogenics* (Springer, New York, 2012), pp. 227–315.

[38] P. Lucas, Mutual friction measurements in uniformly rotating liquid helium, J. Phys. C **3**, 1180 (1970).

[39] J. T. Tough, *Superfluid Turbulence* (North-Holland Publishing Company, Amsterdam, 1982), Chap. 3, pp. 133–219.